

Contents lists available at ScienceDirect

Petroleum Science

journal homepage: www.keaipublishing.com/en/journals/petroleum-science



Original Paper

Heat front propagation in shale oil reservoirs during air injection: Experimental and numerical studies



Shuai Zhao ^{a, b, c, *}, Chun-Yun Xu ^a, Wan-Fen Pu ^a, Qing-Yuan Chen ^a, Cheng-Dong Yuan ^{c, e}, Mikhail A. Varfolomeev ^c. Vladislav Sudakov ^d

- ^a State Key Laboratory of Oil and Gas Reservoir Geology and Exploitation, Southwest Petroleum University, Chengdu, 610500, Sichuan, China
- ^b Tianfu Yongxing Laboratory, Chengdu, 610213, Sichuan, China
- ^c Department of Petroleum Engineering, Kazan Federal University, Kazan, 420008, Russia
- ^d Institute of Geology and Petroleum Technologies, Kazan Federal University, Kazan, 420008, Russia
- ^e Center for Petroleum Science and Engineering, Skolkovo Institute of Science and Technology, Moscow, 121205, Russia

ARTICLE INFO

Article history: Received 20 March 2024 Received in revised form 5 June 2024 Accepted 7 June 2024 Available online 8 June 2024

Edited by Yan-Hua Sun

Keywords: Heat front propagation Shale oil Kinetics model Combustion tube Air injection

ABSTRACT

Air injection technique for developing shale oil has gained significant attention. However, the ability of the heat front to consistently propagate within the shale during air injection remains uncertain. To address this, we investigated the heat front propagation within oil-detritus mixtures, shale cores, and fractured shale cores using a self-designed combustion tube (CT) and experimental schemes. By integrating the results obtained from high-pressure differential scanning calorimetry and CT, we developed a comprehensive reaction kinetics model to accurately analyze the main factors influencing the heat front propagation within fractured shale. The findings revealed that in the absence of additional fractures, the heat front failed to propagate within the tight shale. The flow of gases and liquids towards the shale core was impeded, resulting in the formation of a high-pressure zone at the front region of the shale. This pressure buildup significantly hindered air injection, leading to inadequate oxygen supply and the extinguishment of the heat front. However, the study demonstrated the stable propagation of the heat front within the oil-detritus mixtures, indicating the good combustion activity of the shale oil. Furthermore, the heat front successfully propagated within the fractured shale, generating a substantial amount of heat that facilitated the creation of fractures and enhanced gas injection and shale oil flow. It was important to note that after the heat front passed through the shale, the combustion intensity decreased. The simulation results indicated that injecting air into the main fracturing layers of the shale oil reservoir enabled the establishment of a stable heat front. Increasing the reservoir temperature (from 63 to 143 °C) and oxygen concentration in the injected gas (from 11% to 21%) promoted notable heat front propagation and increased the average temperature of the heat front. It was concluded that temperature and oxygen concentration had the most important influence on the heat front propagation, followed by pressure and oil saturation.

© 2024 The Authors. Publishing services by Elsevier B.V. on behalf of KeAi Communications Co. Ltd. This is an open access article under the CC BY-NC-ND license (http://creativecommons.org/licenses/by-nc-nd/4.0/).

1. Introduction

Shale oil, with its abundant global reserves, holds immense potential for extraction (Liu Y.Z. et al., 2023; Zhou et al., 2023a). However, the implementation of horizontal wells and extensive

E-mail address: zs77816@163.com (S. Zhao).

hydraulic fracturing techniques significantly increases costs (Feng et al., 2020; Jia et al., 2019; Zhao R.B. et al., 2023). Also, the risks associated with water resource shortages and environmental pollution during hydraulic fracturing have always been significant concerns (Scanlon et al., 2022; Zhou et al., 2023b). Numerous experiments and numerical simulations have demonstrated that gas injection can greatly improve shale oil recovery and reduce environmental pollution (Alfarge et al., 2020; Gao et al., 2022; Sheng and Chen, 2014; Wan et al., 2016). Nevertheless, there are practical and economic limitations to current enhanced oil recovery

^{*} Corresponding author. State Key Laboratory of Oil and Gas Reservoir Geology and Exploitation, Southwest Petroleum University, Chengdu, 610500, Sichuan, China.

methods in shale oil reservoirs. CO₂ is often not readily available for use in many cases (Jia and Sheng, 2018). Although hydrocarbon gases are commonly found in oilfields, they are rarely used as injectants due to their market value (Jia et al., 2012). Among the available options, the air injection technique has garnered considerable attention (Jia and Sheng, 2017; Khakimova et al., 2019; Zhang et al., 2020; Zhao et al., 2021a, 2022). This method relies on oxidation reactions and takes advantage of the thermal effect it generates (Alfarge et al., 2020; Chen et al., 2022; Li et al., 2021; Varfolomeev et al., 2016). The shale is subject to high-temperature pyrolysis due to heat release, thus improving its permeability and mesostructure (Wang et al., 2021, 2022; Zhao et al., 2024a).

In recent years, researchers have started investigating the application of air injection for shale oil development. For example, the influence of air injection on shale oil recovery efficiency under varying depletion pressures was studied using a physically simulated method based on computed tomography scanning and nuclear magnetic resonance techniques (Du et al., 2023). Additionally, the microscopic characteristics of pore-throat sizes and the oil recovery mechanism through the air-driven methods were examined. The results demonstrated that a higher oxygen content led to a more pronounced effect of low-temperature oxidation (LTO). With increasing injection pressure, there was a decrease in the lower limit of pore-throat utilization, albeit with the risk of gas channeling and premature breakthrough. Some publications reported that clay minerals present in shale oil reservoirs could act as catalysts, reducing the activation energy barrier and making combustion reactions more favorable (Huang et al., 2016: Jia and Sheng, 2017). Additionally, increasing the oxygen partial pressure enhanced the heat release during shale oil oxidation (Zhao et al., 2021b, 2024b). Jia and Sheng (2018) conducted a simulation study of huff-n-puff air injection in shale oil reservoirs. Their study showed no significant gas override in both air flooding and air huffn-puff injection cases in shale reservoirs. The simulation confirmed that thermal drive was the primary recovery mechanism for huff-npuff air injection. However, the establishment of a stable heat front remains a key challenge in the air injection process, especially in oil reservoirs with low permeability (Bolotov et al., 2023; Cinar and Deniz-Paker, 2023; Zhao S. et al., 2023a). Chen et al. (2018) reported that a higher gas inlet velocity, a smaller equivalence ratio, and a greater initial preheating temperature perturbation could result in a more serious heat front inclination. Actually, it is still uncertain whether the heat front can consistently propagate in tight shale oil reservoirs with complex fractures. These uncertainties have hindered the widespread use of air injection for exploiting shale oil reservoirs.

To address these issues, a study was conducted to investigate the heat front propagation within oil—detritus mixtures, shale cores, and fractured shale cores using a self-designed combustion tube (CT) and experimental schemes. By integrating the results of high-pressure differential scanning calorimetry (HP-DSC) and CT, a comprehensive reaction kinetics model was developed to accurately analyze the main factors influencing the heat front propagation within fractured shale. The combined experimental and numerical results provided valuable insights into the application of the air injection method for shale oil reservoirs with additional fracturing and stimulated further investigations in this field.

2. Experimental

2.1. Materials

The shale oil, brine, and full-diameter shale core (permeability of about 0.01 mD) were sourced from the medium-low maturity shale oil reservoirs (Xinjiang Oilfield, China). The shale core was

crushed to produce detritus with a particle size of 100-120 mesh. The shale oil exhibited a viscosity of 60.1 mPa s at the reservoir temperature (83 °C).

2.2. HP-DSC experiment

The HP-DSC experiments were conducted from 30 to 600 $^{\circ}$ C at 5 MPa. The main procedures included placing about 0.5 mg of the shale oil, setting the constant air flow rate of 30 mL/min, and heating the oil sample at the constant rate of 5 $^{\circ}$ C/min.

2.3. CT experiment

A self-developed fully sealed CT was used to meet the high-temperature and high-pressure conditions for combustion within the shale core. Fig. S1(a)–(c) given in Supporting Information depict the schematic diagram of the CT system, CT, and metal sheath, respectively. The unique feature of this apparatus is its cohesive structure, with a removable metal sheath in the middle for oil sand or core sample filling. The internal cavity of the CT seamlessly aligns with the metal sheath, leaving no gaps. The metal sheath within the CT has an inner diameter of 38 mm and a length of 600 mm. After inserting the core samples, the metal sheath and the CT are welded together for sealing, with only the two ends remaining for external connections. The outer longitudinal wall of the CT is equipped with six fixed metal sheaths, placed at spaced intervals, to accommodate the placement of thermocouples for temperature measurement.

2.3.1. Combustion within the shale core

- (1) The shale oil, brine, and detritus are mixed in a specific mass ratio of 0.98:0.42:8.6.
- (2) To prevent gas channeling during the injection process, it is crucial to ensure close contact between the shale core and the metal, eliminating any gaps. Before loading the shale core, a polishing treatment was applied to its lateral surface, as shown in Fig. S1(d).
- (3) Achieve airtightness by inserting the core into the metal sheath using an interference fit method, as illustrated in Fig. S1(e). Fill other metal sheaths with the oil—detritus mixtures
- (4) Weld and press the different metal sheaths into the CT, placing the core-containing metal sheath in the middle and the metal sheaths with oil—detritus mixtures on either side, as depicted in Fig. S1(f). The thermocouples 1, 2, 5, and 6 are inserted in the surrounding oil—detritus mixtures, and the thermocouples 3 and 4 are inserted in the shale core.
- (5) Close the outlet channel valve and open the inlet channel valve. Begin injecting nitrogen gas. Once the internal pressure within the CT reaches 5 MPa, close the inlet channel valve. Allow the system to settle for 1 h. The gas tightness can be considered satisfactory only when the pressure stabilizes at 5 MPa after 1 h, meeting the experimental requirements.
- (6) Once the sealing at the outlet end of the model is completed, inject nitrogen gas through the gas inlet at the inlet end. Stop the injection when the pressure reaches the designated experimental pressure and simultaneously close the inlet end. After 1 h, if the pressure within the chamber decreases by less than 1%, it is considered to meet the sealing criteria. In case of significant leakage, inspect the leakage points and reseal if necessary.
- (7) The ventilation intensity is set at 40 Nm³/(m² h). Based on the internal diameter of the CT of 38 mm, the cross-sectional area of the internal cavity is calculated to be 1134 mm². This

allows us to determine the injection rate for the experiment, which is 0.75 L/min.

- (8) Set the igniter temperature to 400 °C. Begin heating from the igniter while simultaneously injecting air at the constant rate of 0.75 L/min. Observe and record the values of each thermocouple, analyze the heat front propagation, and collect the produced gases at each stage to analyze changes in their composition.
- (9) Conclude the experiment by discontinuing the injection of nitrogen gas. Close the heating power supply and open the chamber valve to release pressure. Once the temperature drops below 40 °C, the equipment can be dismantled.

Additionally, the CT tests were conducted specifically for the oil—detritus mixtures. The experimental procedures and conditions were identical to those outlined in Section 2.3.1, with the exception of loading core samples.

2.3.2. Combustion within the fractured shale core

- (1) Seal the CT near the outlet end, leaving only the gas outlet for collecting the produced gases through an external pipeline. Fill the CT with oil-detritus mixtures and core samples through the unsealed inlet. When the oil-detritus mixtures are filled to approximately one-third of the lower part of the CT (corresponding to the installation pipe of external thermocouple 5), start placing the core samples. Fill the area around and above the core samples with oil-detritus mixtures and compact it. Repeat this process until the filling reaches two-thirds length of the CT (corresponding to the installation pipe of external thermocouple 3), and then only fill oil-detritus mixtures up to the inlet end face. To ensure the close degree of compaction of the oil-detritus mixtures at both ends of the shale, the experimental procedure involves loading 200 g of the oil-detritus mixtures into a CT, followed by compaction using a sand pressing device under a consistent pressure of 40 MPa. The pressing process is maintained for a duration of 10 min. This sequence is iterated until the oil-detritus mixtures reach the sealing section of the CT, ensuring a systematic and controlled procedure. Once the filling is complete, seal the inlet end of the CT, leaving only the gas inlet for external connection. The distribution of oil—detritus mixtures and shale core samples within the CT is depicted in Fig. S1(g).
- (2) This step corresponds to Steps 5-6 in Section 2.3.1.
- (3) Set the igniter temperature to 400 °C and ignite it within a nitrogen atmosphere. Since the igniter is located near thermocouple 1, when the measured temperature of thermocouple 1 approaches 400 °C, begin injecting air. Observe and record the values of each thermocouple, analyze the heat front propagation, and collect the produced gases at each stage to analyze changes in their composition.
- (4) This step aligns with step 9 in Section 2.3.1.

2.4. Numerical model

2.4.1. Reservoir model

The Computer Modeling Group (CMG) STARS simulator was used to establish a mechanism model (given in Fig. S2 in Supporting Information). The model was constructed with a $25\times25\times5$ grid, with grid dimensions of 3 m \times 3 m \times 2 m. The matrix permeability in the horizontal direction was $1\times10^{-3}~\mu\text{m}^2$, while in the vertical direction, it was $0.12\times10^{-3}~\mu\text{m}^2$. The face-fracturing on the perforation interval was performed using the built-in hydraulic fracturing module in CMG. The fracture permeability was

determined based on equivalent flow capacity and set to $35 \times 10^{-3} \ \mu m^2$ (Han, 2018). The relative permeability curves of the model as shown in Fig. S3 were referenced from the previous study (Bai, 2019). The initial parameter values for the model are presented in Table 1. After setting up the model, air injection development was initiated directly, with an injection rate of 5000 m³/d.

2.4.2. Fluid properties

During the simulation of air injection in shale oil reservoirs, an accurate representation of multiphase fluid flow and the distribution of phase compositions and thermodynamic properties within the fluid system is crucial. By fitting the parameters of the crude oil, the phase behavior simulation using the equation of state can replicate the actual phase changes. The fitting process involves parameters such as crude oil density, bubble point pressure, and viscosity-temperature curve. The aim is to provide state parameters for each fitted component, accurately representing the characteristics of oil samples. Table 2 lists the basic parameters of components in the model.

2.4.3. Reaction schemes

The reaction equations include (1) oxygenation of heavy components (see reaction 1), (2) cracking of hydrocarbon oxidants (see reaction 2), and (3) combustion of light components, heavy components, and coke (see reactions 3–5). Table 3 shows the determined reaction parameters for each reaction equation.

Heavy fraction
$$+ 1.5O_2 \rightarrow 0.85$$
 oxidized oil $+ CO_2 + H_2O$ (1)

Oxidized oil
$$\rightarrow$$
 3.8light fraction + 1.2coke (2)

Light fraction
$$+0.52O_2 \rightarrow 9.88H_2O + 2.29CO_2 + 6.59CO$$
 (3)

Heavy fraction
$$+25.03O_2 \rightarrow 22.32H_2O + 6.42CO_2 + 14.89CO$$
 (4)

$$Coke + 1.08O_2 \rightarrow 0.5H_2O + 0.67CO_2 + 0.33CO$$
 (5)

2.4.4. Fitting of HP-DSC and CT data

The HP-DSC grid system as shown in Fig. S4 was constructed according to the method reported previously (Huang and Sheng, 2017a, 2017b). The CT model was built to precisely represent its actual shape and size. The parameter settings of the HP-DSC and CT models were the same with those of the experiments stated in Sections 2.2 and 2.3. To fit the HP-DSC and CT data, adjustments were made to the kinetic parameters, stoichiometric numbers, and reaction enthalpy of reactions 1 to 5. Fig. 1(a) and (b) display the experimental and fitted results of HP-DSC and CT. The fitting results

Table 1Basic parameters used in the reservoir model.

Parameter	Value
Porosity, %	15
Vertical permeability, mD	0.12
Horizontal permeability, mD	1
Rock thermal conductivity, J/(m day °C)	2.07×10^{5}
Water thermal conductivity, J/(m day °C)	5.35×10^{4}
Oil thermal conductivity, J/(m day °C)	1.5×10^5
Gas thermal conductivity, J/(m day °C)	4×10^3
Rock volumetric heat capacity, J/(m ³ °C)	1.85×10^{5}
Thermal conductivity of over/under burden rock, J/(cm min °C)	2.07×10^{5}
Volumetric heat capacity of over/under burden rock, J/(m ³ °C)	1.85×10^{5}

Table 2Basic parameters of components in the model.

Parameter	Component						
	$\overline{O_2}$	CO ₂	N ₂	CH ₄	Light fraction	Heavy fraction	H ₂ O
Molar weight, g/mol	32	44	28	16	301.2	618.2	18
Critical temperature, °C	-118.6	31.1	-147.0	-82.6	377.4	551.89	374.2
Critical pressure, kPa	5046	7376	3394	4600	20107	11990.87	22129
Acentric factor	0.019	0.225	0.04	0.008	0.21	0.87	0.344
Q_{a}	0.457	0.457	0.457	0.457	0.457	1.001	0.457
Q_{b}	0.078	0.078	0.078	0.078	0.078	0.063	0.078
V _c , L/mol	0.091	0.094	0.090	0.099	0.486	1.091	0.056
V _c (viscosity), L/mol	0.091	0.094	0.09	0.099	0.494	1.1	0.056
Z (Rackett)	0.289	0.274	0.291	0.288	0.31	0.272	0.234

Table 3Reaction parameters for each reaction equation.

Reaction	Frequency factor, min ⁻¹	Activation energy, J/mol	Heat enthalpy, J/mol
1	1.39×10^{12}	53.3 × 10 ³	9.4×10^{3}
2	2.36×10^{12}	120×10^{3}	0
3	2.48×10^{9}	82.4×10^{3}	6.8×10^{6}
4	3.34×10^{9}	135×10^{3}	2.2×10^{7}
5	6.80×10^9	74.5×10^3	2.4×10^5

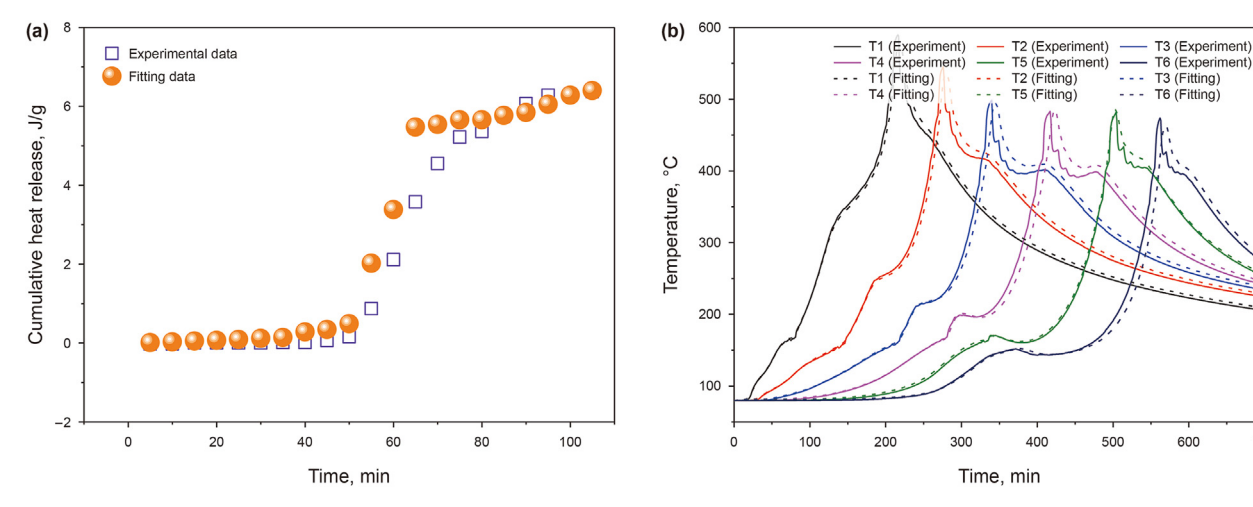


Fig. 1. Experimental and fitted results (T1-T6 represent thermocouples 1-6 in Fig. S1 in Supporting Information). (a) HP-DSC; (b) CT for the oil-detritus mixtures.

closely resembled the experimental ones, indicating that the established reaction kinetics model simulated the exothermic characteristics of shale oil oxidation successfully.

3. Results and discussion

3.1. Analysis of the experimental results of CT

Fig. 2(a) illustrates the temperature changes over time at each thermocouple. The temperature of all thermocouples showed a gradual increase over time. Meanwhile, the pressure difference continued to rise until it reached 9.5 MPa. Concurrently, the flow rates at the outlet end steadily declined, with the gas flow rate reaching 0.12 L/min. These observations indicated the occurrence of serious plugging effect within the CT. The combustion experiment was conducted for approximately 7 h. According to the real-time temperature monitoring system, thermocouple 1, positioned at the ignition section, consistently measured a temperature of 240 °C. Thermocouple 2, located at the front end of the shale core, showed fluctuations within the range of 185±3 °C. Thermocouples

3 and 4, representing different sections of the shale core, recorded temperatures of 168 and 150 $^{\circ}$ C, respectively. At this stage, the temperatures in all sections had nearly reached a plateau, leading to the decision to end the experiment.

700

Fig. 2(b) shows the concentration changes of produced gases during air injection. A small amount of H_2 , CH_4 , and trace amounts of CO_2 were detected in the produced gas when the temperature of thermocouple 1 reached 150 °C. The oxygen content experienced a decrease of less than 1%. As the temperature of thermocouple 1 reached 240 °C, the oxygen content in the produced gas sharply decreased, and the CO_2 content significantly rose. This indicated the occurrence of combustion where a portion of the crude oil and oxygen reacted vigorously, resulting in the production of CO_2 and H_2O . Furthermore, there was a notable increase in CH_4 , suggesting the decomposition of heavy components and the generation of light hydrocarbon components within the combustion zone.

Fig. 2(c) shows the post mortem for combustion. From left to right: the leftmost portion corresponds to the oil—detritus mixtures near the igniter, with temperature data corresponding to thermocouple 1; the middle portion represents the oil—detritus

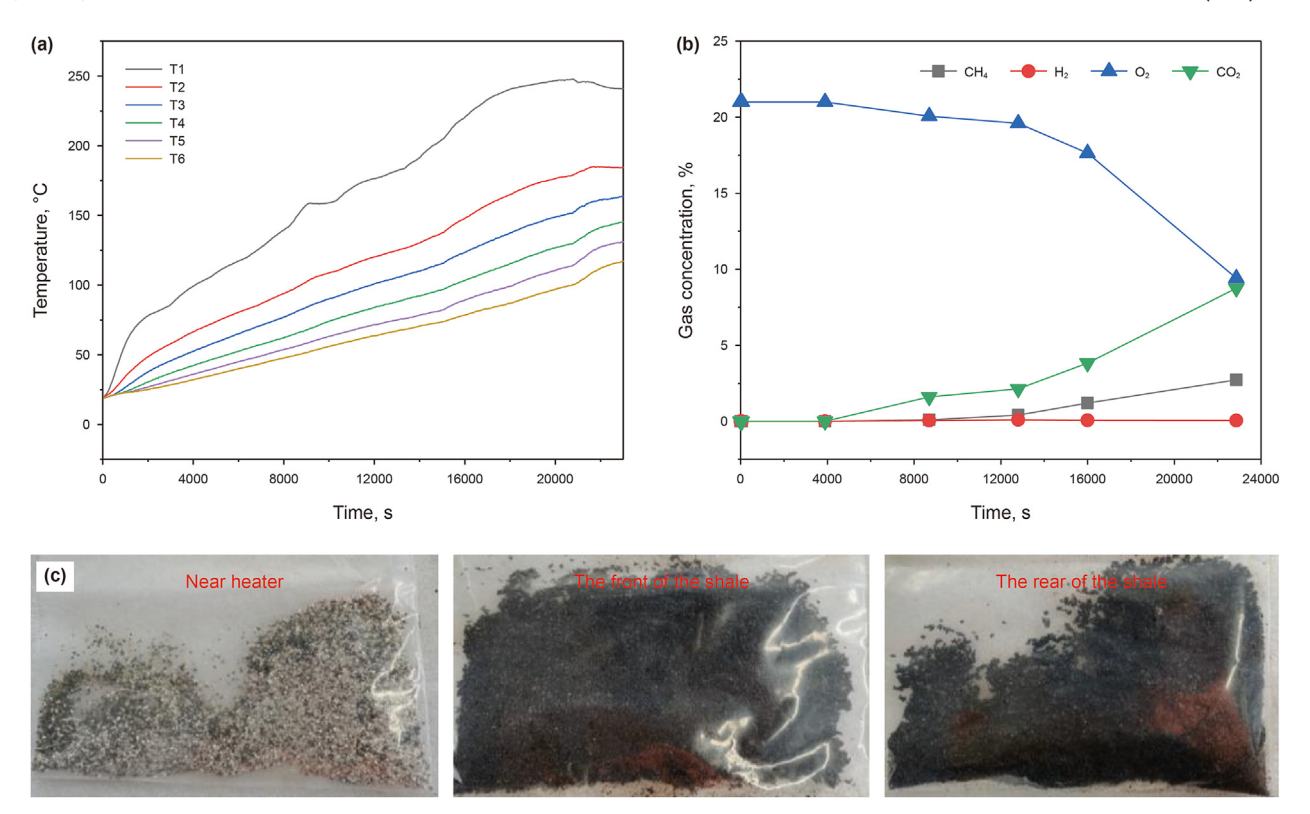


Fig. 2. (a) Temperature curves for combustion within the shale core; (b) Concentration curves of produced gases for combustion; (c) Post mortems for combustion.

mixtures near the front end of the core, with temperature data corresponding to thermocouple 2; the rightmost portion depicts the oil—detritus mixtures near the back end of the core, with temperature data corresponding to thermocouples 5 and 6. It was evident that complete combustion of the crude oil occurred only in the oil—detritus mixtures near the igniter. In contrast, only trace amounts of crude oil depletion could be observed in the oil—detritus mixtures near the back end of the core.

Throughout the experimental process, there were no significant abrupt increases in temperature. The temperatures recorded by the thermocouples exhibited a slow and gradual rise, reaching a certain temperature and then ceasing to increase further. Upon examining the condition of the oil-detritus mixtures and core in different parts of the combustion chamber after the experiment, only the area near the ignition site showed some resemblance to the combusted zone described in the previous publications (Liu Z.Z. et al., 2023; Kovscek et al., 2013; Zhao et al., 2015). It therefore was concluded that only the ignition section experienced a short period of combustion, resulting in the formation of secondary steam and flue gas. However, as the heat front propagated toward the shale core, it pushed the coking zone forward. The injected air, flue gas, and the mixed fluid formed by combustion were pushed to the front end region of the shale core. The advancement of the coking zone also caused a decrease in the permeability of the shale core at the front end. Moreover, due to the high density of shale itself, the mixed fluid could not pass through quickly under the current flow rate. This directly led to the gradual formation of a high-pressure zone at the front end of the shale, greatly impeding the flow of air, flue gas, secondary steam, and heat. The formation of the highpressure zone blocked the passage of air, resulting in a lack of oxygen in the combustion zone. Consequently, an effective heat source failed to be sustained. This explained why the heat front failed to pass through the shale core. Simultaneously, as shown in Fig. 1(b), the heat front propagated stably within the oil—detritus mixtures, which suggested that the shale oil showed the good combustion activity. Given the afore-mentioned results, it was necessary to further explore the heat front propagation within the fractured shale.

Fig. 3(a) shows the temperature curves for combustion within the fractured shale core. When the temperature recorded by thermocouple 1 reached 300 °C, the increasing rate of temperature slowed down. Upon reaching the ignition temperature of 400 °C, continuous air injection was initiated. It was apparent that after reaching 400 °C, the combustion reactions occurred between oil-detritus mixtures and oxygen within the CT. This combustion released a substantial amount of heat, leading to a rapid increase in temperature observed by thermocouple 1, increasing to 600 °C. As the fuel was consumed and the combustion could no longer proceed, the combustion ended, resulting in a swift decrease in temperature at thermocouple 1. However, due to the thermal compensation provided by the igniter, the temperature remained relatively stable (around 400 °C). Simultaneously, the abundant heat generated by combustion facilitated the heat front propagation, as indicated by the increase in temperatures measured by thermocouples 2, 3, and 4.

In the vicinity of thermocouple 2, the fuel was produced through a series of complex LTO and thermo-oxidative cracking reactions as reported previously (Hascakir et al., 2013; Xu et al., 2018; Zhao et al., 2021a). As the temperature rose to a certain level, the combustion reactions ensued. Subsequently, as the combustion reactions ended and the fuel was exhausted, the temperature rapidly declined. However, the temperature stabilized at around 300 °C

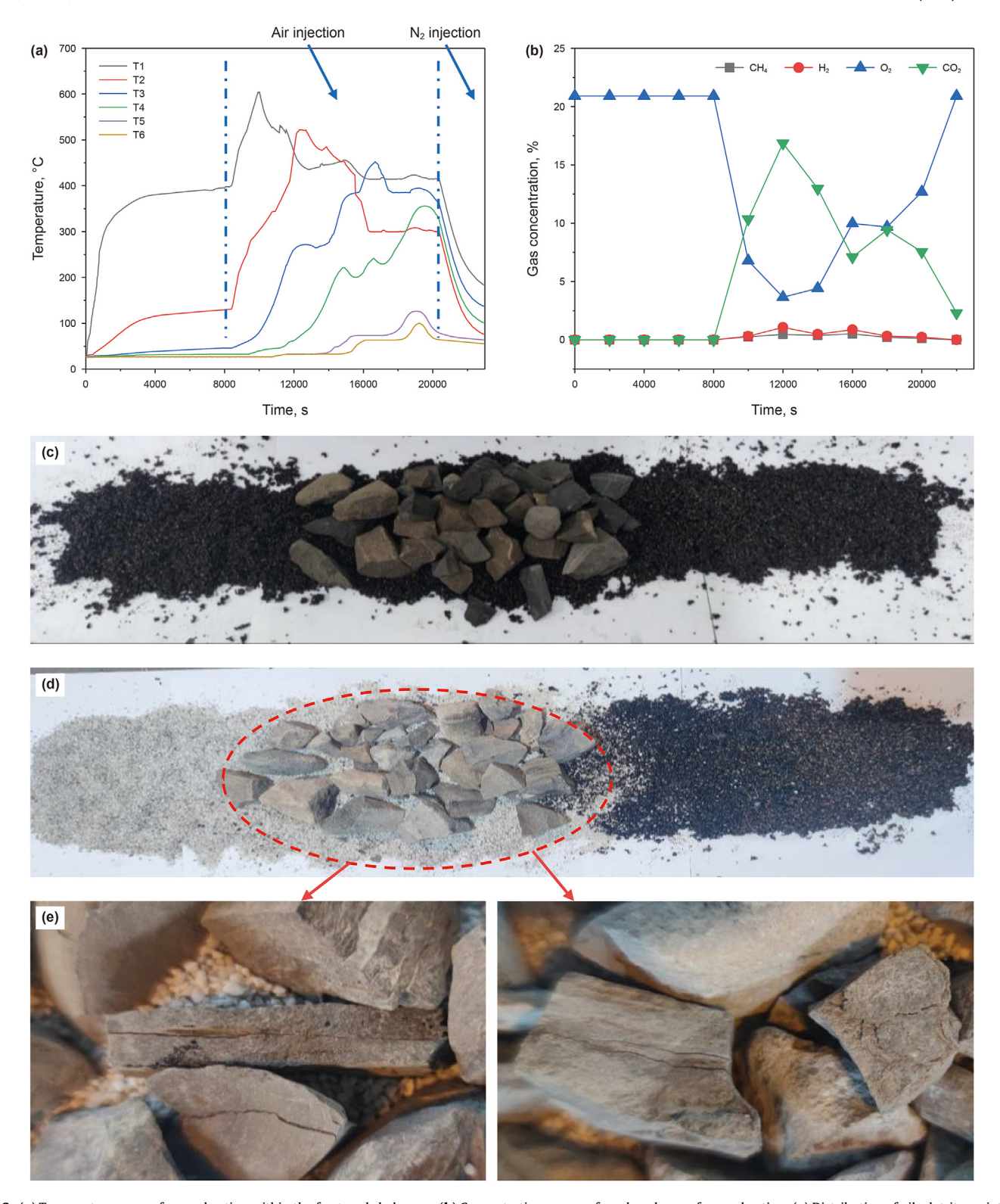


Fig. 3. (a) Temperature curves for combustion within the fractured shale core; (b) Concentration curves of produced gases for combustion; (c) Distribution of oil—detritus mixtures and fractured shale before combustion; (d) Post mortems for combustion; (e) Enlarged picture of the shale core with obvious fractures.

due to the heat compensation from the region of thermocouple 1. Notably, the oil bank was formed in the vicinity of thermocouples 3 and 4, while thermocouples 5 and 6 represented the cold oil region.

Due to the presence of core samples in the area of thermocouples 3 and 4, combined with the low permeability of the oil bank, the combustion intensity gradually increased as the heat front

propagated. However, the influence of the heat front had not completely dissipated, and the temperature continued to propagate forward through thermal conduction. Hence, thermocouples 3 and 4 maintained a relatively high temperature level.

Fig. 3(b) shows a rapid decrease in the oxygen concentration after injecting air. This decrease was attributed to the occurrence of intense combustion reactions as mentioned previously. During combustion, the heavier hydrocarbons gradually transformed into lighter cycloalkanes and organic compounds with aromatic structures. CH₄ began to evolve when the temperature reached a level capable of overcoming intermolecular forces. It indicated that the thermal energy became sufficient to break the bonds of the heavier hydrocarbon molecules, resulting in the formation of lighter hydrocarbons (Freitag, 2016; Sheng and Yang, 2024; Yuan et al., 2022). Overall, the changes in gas composition observed in Fig. 3(b) indicated the occurrence of various chemical reactions, including oxidation, cracking, and decomposition, leading to the generation of lighter hydrocarbons, oxygenated derivatives, and CO₂.

Fig. 3(c) shows the distribution of oil—detritus mixtures and fractured shale before combustion, and Fig. 3(d) shows the post mortem for combustion. It was observed that the black color of oil—detritus mixtures and shale cores in the corresponding regions of thermocouples 1 to 4 transitioned to a white state, indicating the stable heat front propagation. Furthermore, as shown in Fig. 3(e), visual fractures could be observed on some cores obtained from the regions where thermocouples 3 and 4 were placed. These fractures could enhance the permeability of the shale, facilitating the injection and flow of gases and shale oil within the reservoir.

3.2. Analysis of the main factors affecting the heat front propagation

Fig. 4 shows the reservoir temperature distributions under initial temperatures of 63, 103, and 143 °C. Fig. 5 shows the reservoir temperature and oil saturation distributions in the 4th month. There was a gradual increase in the progression of heat front as the reservoir temperature rose. Notably, at a reservoir temperature of 143 °C, the diffusion zone of the heat front expanded noticeably within the range of 350–450 °C. Examining the distribution of oil saturation, it became apparent that the oil bank zone exhibited higher oil saturation with increasing reservoir temperature.

Similarly, an analysis of the temperature and oil saturation fields running until the 4th month (refer to Fig. 6) indicated comparable average temperatures and propagation distances of the heat front for oil saturation of 60%, 70%, and 80%. Additionally, the frontal region of the heat front formed the oil bank with oil saturation higher than 80%. This occurrence was due to the substantial heat released during oxidation, resulting in a rapid decrease in crude oil viscosity within the frontal region and the accumulation of upgraded oil, thus forming the oil bank.

Fig. 7 shows the distribution of temperature and oil saturation fields for different oxygen concentrations (11%, 16%, and 21%) in the 4th month. The results clearly demonstrated the significant influence of oxygen concentration on the heat front propagation, with a faster propagation observed at an oxygen concentration of 21%. The average temperatures of the heat front for oxygen concentrations of 21%, 16%, and 11% were 413, 331, and 256 °C, respectively. This

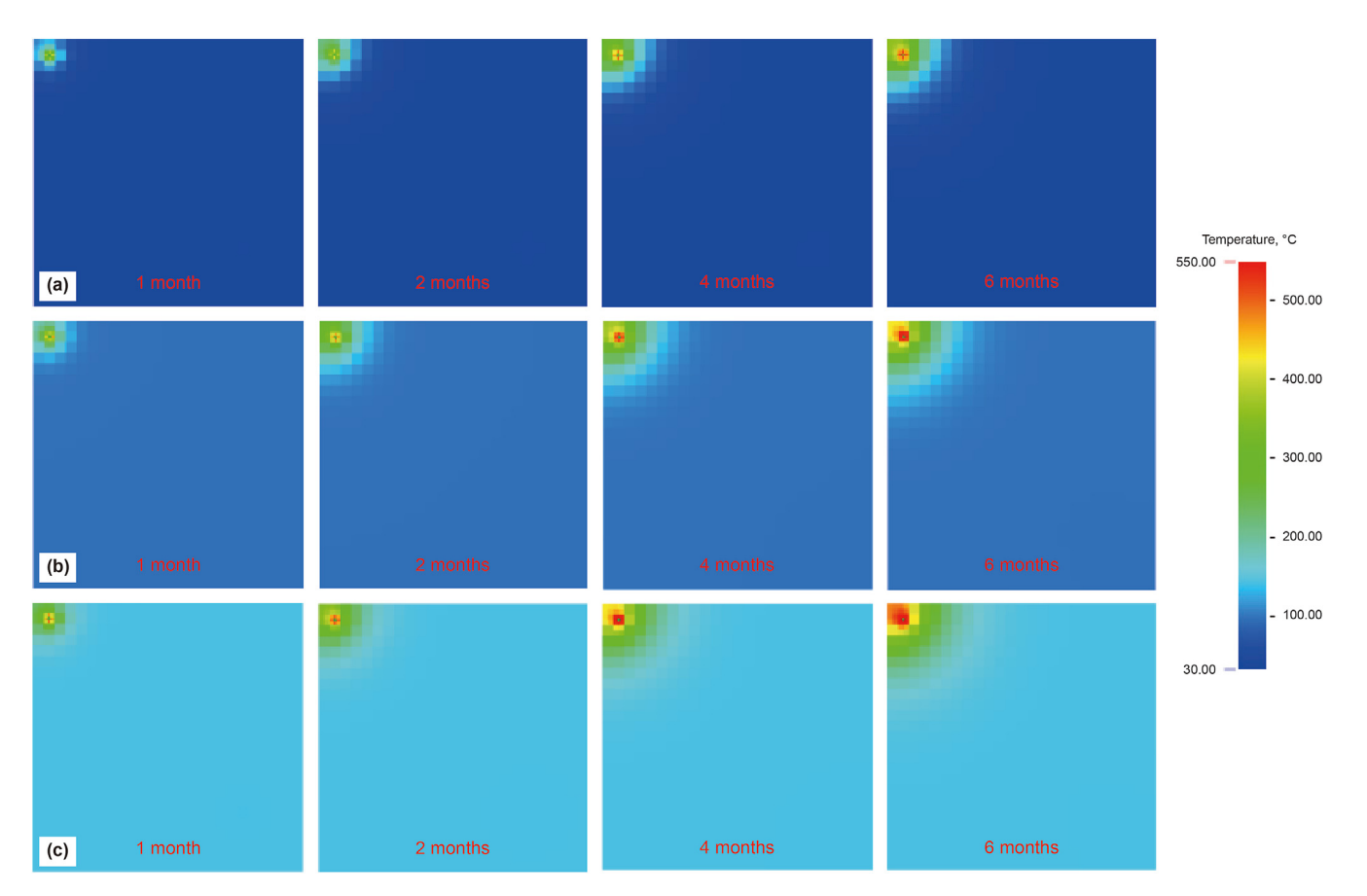


Fig. 4. Reservoir temperature distributions under different initial temperatures of 63 °C (a), 103 °C (b), and 143 °C (c), respectively.

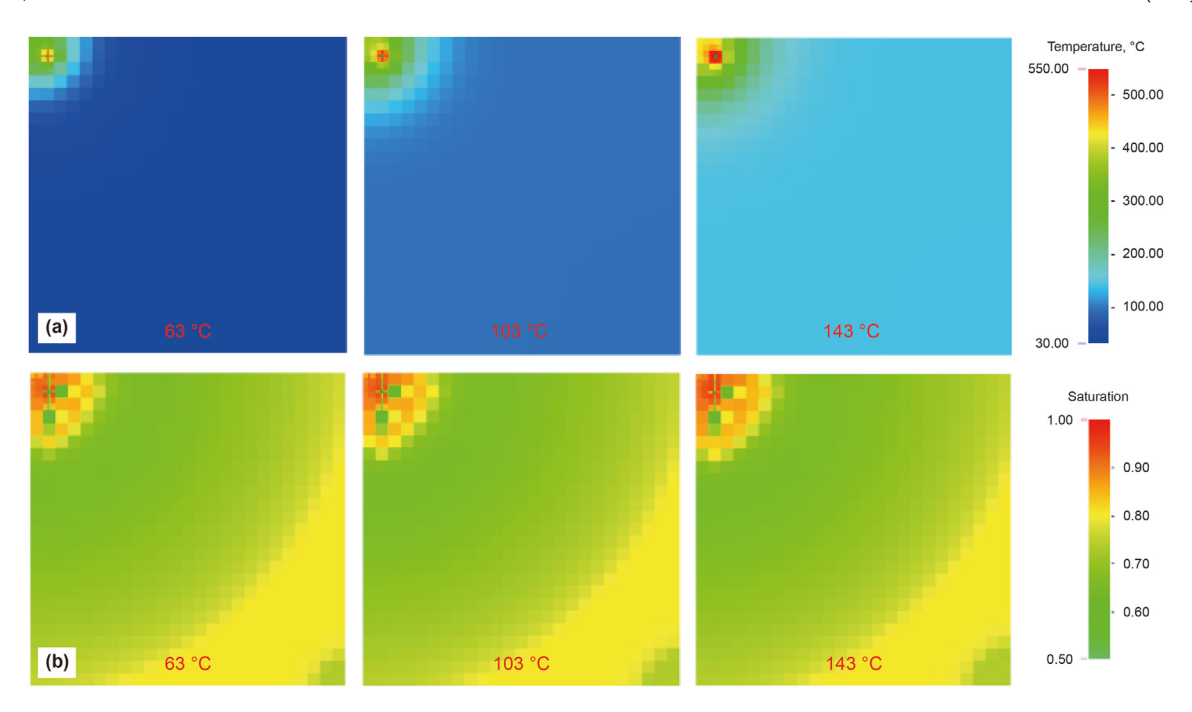


Fig. 5. Distributions of reservoir temperature (a) and oil saturation (b) in the 4th month under different initial temperatures.

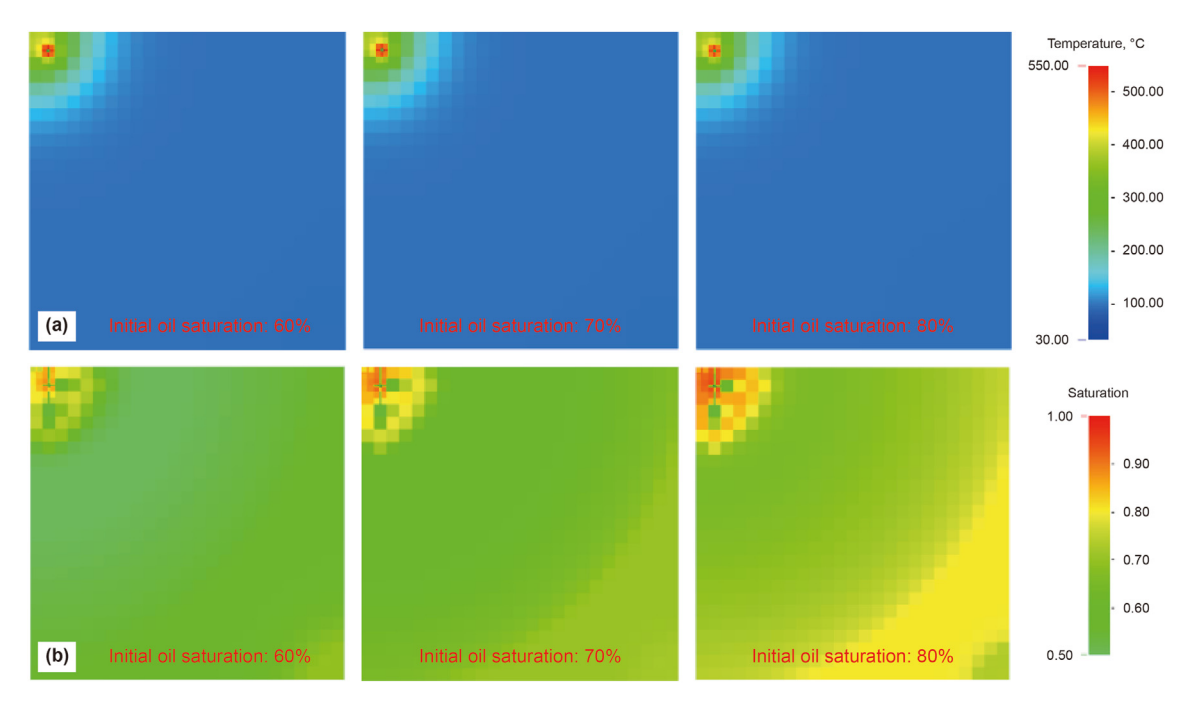


Fig. 6. Distributions of reservoir temperature (a) and oil saturation (b) under different initial oil saturation.

phenomenon indicated that an increase in oxygen concentration effectively enhanced the oxidation rate and heat release, consistent with the previous findings (Jia et al., 2016; Jiang et al., 2019; Zhao S. et al., 2023b). Moreover, the oil saturation field revealed a progressive increase in oil saturation in the outermost layer of the oil bank as the oxygen concentration rose. This was attributed to the heightened collision frequency between molecules during oxidation, leading to strengthened exothermic oxidation reactions and the accumulation of upgraded oil at the front end of the heat front. Fig. 8 depicts the distributions of temperature and oil saturation

fields for different pressures in the 4th month. It was evident that pressure had minimal impact on the heat front. The distributions of the temperature and oil saturation fields remained similar across different pressures.

3.3. Evaluation of the main factors affecting the heat front propagation using the grey correlation method

The numerical modeling results were further evaluated using the grey correlation method to rank the influencing factors. The

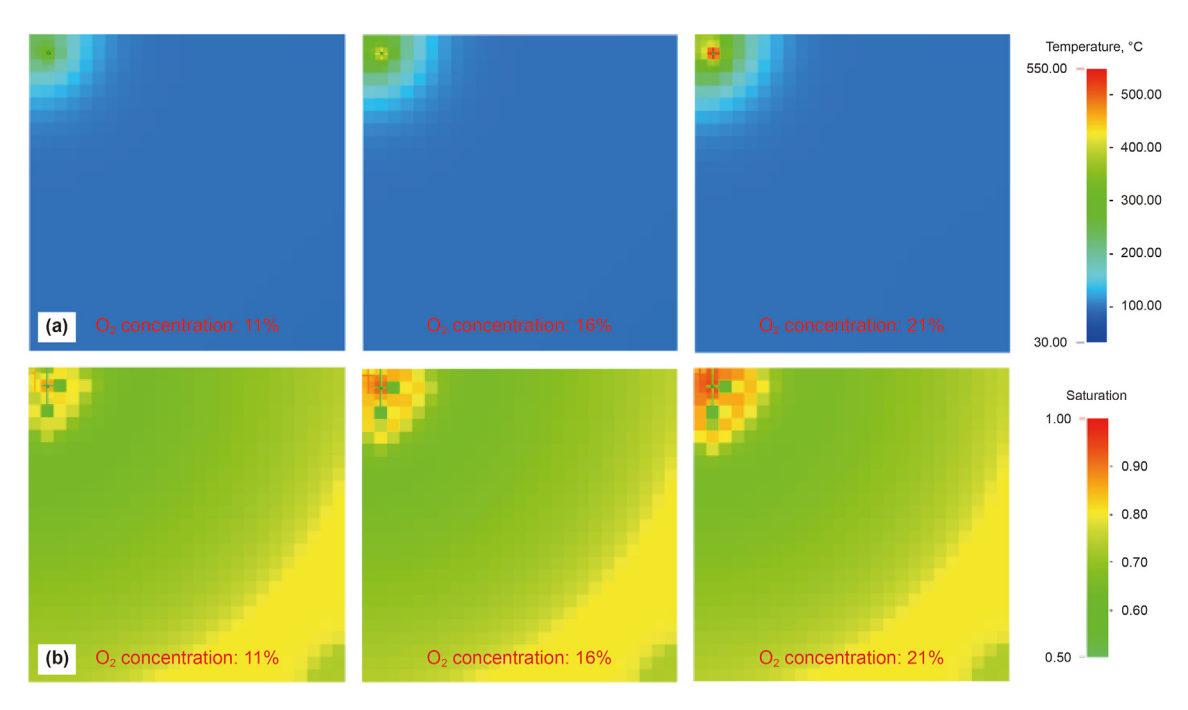


Fig. 7. Distributions of reservoir temperature (a) and oil saturation (b) in the 4th month under different O_2 concentrations.

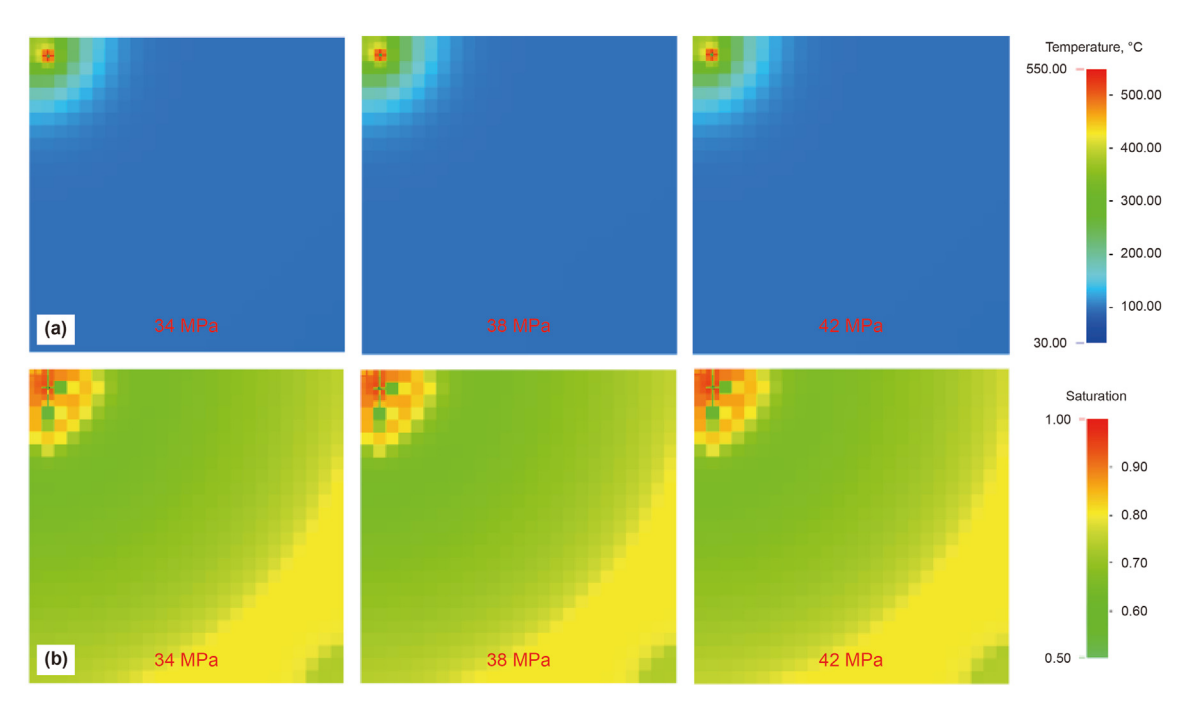


Fig. 8. Distributions of reservoir temperature (a) and oil saturation (b) in the 4th month under different initial pressures.

average temperature of the heat front served as the reference sequence for the analysis. Initially, the data was normalized using the initial value method, with the average temperature of the heat front as the reference mother sequence (X_0), and other data, such as the reservoir temperature, considered as comparative subsequences (X_i). X_1 — X_4 represented the temperature, oil saturation, oxygen concentration, and pressure, respectively. The results of the data preprocessing were found in Table 4. Subsequently, the absolute differences (ΔX_i) between the mother sequence and each comparative subsequence were calculated, as shown in Table 5. The maximum and minimum absolute differences were determined to

be $\Delta max = 0.28$ and $\Delta min = 0$, respectively.

Table 6 lists the correlation coefficients (r_i) between the mother sequence and the comparative subsequence, which were calculated using Eq. (6).

$$r(x_0(k),x_i(k)) = \frac{m+\xi M}{\Delta_0(k)+\xi M} \tag{6}$$

where m is the minimum difference; M is the maximum difference; and ξ is the resolution coefficient, commonly set at 0.5.

Applying Eq. (7), the correlation degrees (β_1 , β_2 , β_3 , and β_4) for

Table 4 Preprocessing of data.

X_0	X_1	X_2	X_3	<i>X</i> ₄
1.00	1.00	1.00	1.00	1.00
0.80	0.76	1.00	1.00	1.00
1.17	1.24	1.00	1.00	1.00
1.03	1.00	0.75	1.00	1.00
1.02	1.00	0.88	1.00	1.00
0.78	1.00	1.00	0.52	1.00
0.82	1.00	1.00	0.76	1.00
1.00	1.00	1.00	1.00	0.94
1.00	1.00	1.00	1.00	1.06

 Table 5

 Absolute differences between the mother sequence and each comparative subsequence.

<i>X</i> ₀	X_1	<i>X</i> ₂	<i>X</i> ₃	<i>X</i> ₄
1.00	0.00	0.00	0.00	0.00
0.80	0.04	0.20	0.20	0.20
1.17	0.07	0.17	0.17	0.17
1.03	0.03	0.28	0.03	0.03
1.02	0.02	0.14	0.02	0.02
0.78	0.22	0.22	0.26	0.22
0.82	0.18	0.18	0.06	0.18
1.00	0.00	0.00	0.00	0.06
1.00	0.00	0.00	0.00	0.06

Table 6Correlation coefficients between the mother sequence and the comparative subsequence.

<i>X</i> ₀	X_1	X_2	<i>X</i> ₃	X_4
1.00	1.00	1.00	1.00	1.00
0.80	0.75	0.42	0.42	0.42
1.17	0.67	0.45	0.45	0.45
1.03	0.81	0.33	0.81	0.81
1.02	0.90	0.50	0.90	0.90
0.78	0.39	0.39	0.35	0.39
0.82	0.44	0.44	0.70	0.44
1.00	1.00	1.00	1.00	0.72
1.00	1.00	1.00	1.00	0.72

each parameter were determined as 0.77, 0.62, 0.74, and 0.65, respectively. Thus, the order of correlation degrees was as follows: temperature > oxygen concentration > pressure > oil saturation. In summary, for shale oil reservoirs, injecting air at higher reservoir temperatures effectively promoted the heat front propagation.

$$\beta_i = \frac{1}{n} \sum_{j=1}^{n} r(x_0(k), x_i(k)) \tag{7}$$

4. Conclusions

In this work, the heat front propagation within oil—detritus mixtures, shale cores, and fractured shale cores was investigated using a self-designed CT and experimental schemes. A comprehensive reaction kinetics model was then developed by integrating the HP-DSC and CT results, with the objective of analyzing the main factors influencing the heat front propagation within fractured shale accurately. The significant conclusions were as drawn follows.

(1) The heat front failed to propagate within the tight shale without additional fractures. The flow of the gases and liquids towards the shale core was hindered, resulting in the

- formation of a high-pressure zone in the front region of the shale core. This pressure buildup greatly reduced air injection, leading to insufficient oxygen supply and extinguishment of the heat front.
- (2) The stable heat front propagation within the oil—detritus mixtures indicated that the shale oil had the good combustion activity. The heat front could propagate within the fractured shale, during which a large amount of heat release could generate fractures in shale, facilitating gas injection and shale oil flow. Simultaneously, it should be pointed out that after the heat front passed through the shale, the combustion intensity decreased.
- (3) The simulation results indicated that the injection of air into the main fracturing layers of the shale oil reservoir enabled the establishment of a stable heat front, which was expected to significantly enhance oil recovery.
- (4) With an increase in reservoir temperature (from 63 to 143 °C), the heat front propagated notably. Higher oxygen concentrations in the injected gas (from 11% to 21%) promoted the heat front propagation and increased the average temperature of the heat front.
- (5) Employing the grey correlation method, it was concluded that temperature and oxygen concentration generated the most significant influence on the heat front propagation, followed by pressure and oil saturation.

CRediT authorship contribution statement

Shuai Zhao: Writing — original draft, Resources, Methodology, Funding acquisition, Conceptualization. **Chun-Yun Xu:** Methodology, Investigation, Formal analysis. **Wan-Fen Pu:** Supervision, Methodology. **Qing-Yuan Chen:** Validation, Software, Formal analysis. **Cheng-Dong Yuan:** Writing — review & editing, Validation. **Mikhail A. Varfolomeev:** Methodology, Funding acquisition. **Vladislav Sudakov:** Software.

Declaration of competing interest

The authors declare that they have no known competing financial interests or personal relationships that could have appeared to influence the work reported in this paper.

Acknowledgements

This work was supported by National Natural Science Foundation of China (No. 52204049), Natural Science Foundation of Sichuan Province (No. 2024NSFSC0960), and Ministry of Science and Higher Education of the Russian Federation under Agreement No. 075-15-2022-299 within the Framework of the Development Program for a World-Class Research Center "Efficient development of the global liquid hydrocarbon reserves". The authors thank CMG for providing the simulators to Kazan Federal University.

Appendix A. Supplementary data

Supplementary data to this article can be found online at https://doi.org/10.1016/j.petsci.2024.06.005.

References

Alfarge, D., Wei, M., Bai, B., 2020. Air injection in shale and tight oil reservoirs. Dev. Petrol. Sci. 67, 87–111. https://doi.org/10.1016/B978-0-12-818343-4.00005-X. Bai, J., 2019. Research and Application of CO₂ Huff and Puff in Tight Oil. Master Thesis. China University of Petroleum, Beijing (in Chinese).

technique for developing fractured low permeable oil shale: experimental evidence for synthetic oil generation and successful propagation of combustion front. Fuel 344, 127995. https://doi.org/10.1016/j.fuel.2023.127995.

- Chen, C., Tang, X., Qin, M., et al., 2022. Experimental evaluation of shale oil development effectiveness by air injection. Energies 15, 9513. https://doi.org/10.3390/en.15249531.
- Chen, L., Xia, Y.F., Li, B.W., et al., 2018. Flame front inclination instability in the porous media combustion with inhomogeneous preheating temperature distribution. Appl. Therm. Eng. 128, 1520–1530. https://doi.org/10.1016/j.applthermaleng.2017.09.085,
- Cinar, M., Deniz-Paker, M., 2023. Laboratory experiments of in situ combustion in core samples with simulated fractures. J. Petrol. Sci. Eng. 220, 111153. https:// doi.org/10.1016/j.petrol.2022.111153.
- Du, M., Lv, W.F., Yang, Z.M., et al., 2023. An online physical simulation method for enhanced oil recovery by air injection in shale oil. Petrol. Explor. Dev. 50 (4), 909–923. https://doi.org/10.1016/S1876-3804(23)60437-9.
- Feng, Q.H., Xu, S.Q., Xing, X.D., et al., 2020. Advances and challenges in shale oil development: a critical review. Advances in Geo-Energy Research 4 (4), 406–418. https://doi.org/10.46690/ager.2022.04.06.
- Freitag, N.P., 2016. Chemical reaction mechanisms that govern oxidation rates during in-situ combustion and high-pressure air injection. SPE Reservoir Eval. Eng. 19, 645–654. https://doi.org/10.2118/170162-PA.
- Gao, Y., Wan, T., Dong, Y., et al., 2022. Numerical and experimental investigation of production performance of in-situ conversion of shale oil by air injection. Energy Rep. 8, 15740–15753. https://doi.org/10.1016/j.egyr.2022.08.174.
- Han, W., 2018. Research on the Effect of CO₂ Huff and Puff of Fractured Horizontal Wells in Tight Oil Reservoirs. Master Thesis. China University of Petroleum, Beijing (in Chinese).
- Hascakir, B., Ross, C.M., Castanier, L.M., et al., 2013. Fuel formation and conversion during in-situ combustion of crude oil. SPE J. 18 (6), 1217–1228. https://doi.org/ 10.2118/146867-PA.
- Huang, S.Y., Jia, H., Sheng, J.J., 2016. Effect of shale core on combustion reactions of tight oil from Wolfcamp reservoir. Petrol. Sci. Technol. 34 (13), 1172–1179. https://doi.org/10.1080/10916466.2016.1185441.
- Huang, S.Y., Sheng, J.J., 2017a. A practical method to obtain kinetic data from TGA (thermogravimetric analysis) experiments to build an air injection model for enhanced oil recovery. Fuel 206, 199–209. https://doi.org/10.1016/ j.fuel.2017.06.019.
- Huang, S.Y., Sheng, J.J., 2017b. An innovative method to build a comprehensive kinetic model for air injection using TGA/DSC experiments. Fuel 210, 98–106. https://doi.org/10.1016/j.fuel.2017.08.048.
- Jia, B., Tsau, J.S., Barati, R., 2019. A review of the current progress of CO₂ injection EOR and carbon storage in shale oil reservoirs. Fuel 236, 404–427. https:// doi.org/10.1016/j.fuel.2018.08.103.
- Jia, H., Liu, P.G., Pu, W.F., et al., 2016. In situ catalytic upgrading of heavy crude oil through low-temperature oxidation. Petrol. Sci. 13, 476–488. https://doi.org/ 10.1007/s12182-016-0113-6.
- Jia, H., Sheng, J.J., 2017. Discussion of the feasibility of air injection for enhanced oil recovery in shale oil reservoirs. Petroleum 3 (2), 249–257. https://doi.org/ 10.1016/j.petlm.2016.12.003.
- Jia, H., Sheng, J.J., 2018. Simulation study of huff-n-puff air injection for enhanced oil recovery in shale oil reservoirs. Petroleum 4 (1), 7–14. https://doi.org/10.1016/ i.petlm.2017.09.006.
- Jia, H., Zhao, J.Z., Pu, W.F., et al., 2012. Thermal study on light crude oil for application of high-pressure air injection (HPAI) process by TG/DTG and DTA tests. Energy & Fuels 26 (3), 1575–1584. https://doi.org/10.1021/ef201770t.
- Jiang, H., Yang, J.Y., Huang, J., et al., 2019. Heat release model for the low temperature oxidation of heavy oils from experimental analyses and numerical simulations. Energy & Fuels 33 (5), 3970–3978. https://doi.org/10.1021/acs.energyfuels.8b04506.
- Khakimova, L., Bondarenko, T., Cheremisin, A., et al., 2019. High pressure air injection kinetic model for Bazhenov Shale Formation based on a set of oxidation studies. J. Petrol. Sci. Eng. 172, 1120–1132. https://doi.org/10.1016/j.petrol.2019.09.021.
- Kovscek, A.R., Castanier, L.M., Gerritsen, M.G., 2013. Improved predictability of insitu-combustion enhanced oil recovery. SPE Reservoir Eval. Eng. 16 (2), 172–182. https://doi.org/10.2118/165577-PA.
- Li, Y.B., Lin, X., Gao, Z.W., et al., 2021. The comprehensive investigation of the improvement of shale formation property in high pressure air injection. In: SPE/ AAPG/SEG Asia Pacific Unconventional Resources Technology Conference. https://doi.org/10.15530/ap-urtec-2021-208371.
- Liu, Y.Z., Zeng, J.H., Qiao, J.C., et al., 2023. An advanced prediction model of shale oil production profile based on source-reservoir assemblages and artificial neural networks. Appl. Energy 333, 120604. https://doi.org/10.1016/

j.apenergy.2022.120604.

- Liu, Z.Z., Pu, W.F., Zhao, X.G., et al., 2023. Combustion tube experiments on key factors controlling the combustion process of air injection with light oil reservoir. Geoenergy Science and Engineering 224, 211611. https://doi.org/10.1016/ i.geoen.2023.211611.
- Scanlon, B.R., Reedy, R.C., Wolaver, B.D., 2022. Assessing cumulative water impacts from shale oil and gas production: permian Basin case study. Sci. Total Environ. 811, 152306. https://doi.org/10.1016/j.scitotenv.2021.152306.
- Sheng, J.J., Chen, K., 2014. Evaluation of the EOR potential of gas and water injection in shale oil reservoirs. Journal of Unconventional Oil and Gas Resources 5, 1–9. https://doi.org/10.1016/j.juogr.2013.12.001.
- Sheng, J.J., Yang, E.L., 2024. An analytical model to estimate the time delay to reach spontaneous ignition considering heat loss in oil reservoirs. Petrol. Sci. https://doi.org/10.1016/j.petsci.2024.01.011
- Varfolomeev, M.A., Galukhin, A., Nurgaliev, D.K., et al., 2016. Thermal decomposition of Tatarstan Ashal'cha heavy crude oil and its SARA fractions. Fuel 186, 122–127. https://doi.org/10.1016/j.fuel.2016.08.042.
- Wan, T., Sheng, J., Soliman, M.Y., et al., 2016. Effect of fracture characteristics on behavior of fractured shale-oil reservoirs by cyclic gas injection. SPE Reservoir Eval. Eng. 19 (2), 350–355. https://doi.org/10.2118/168880-PA.
- Wang, L., Yang, D., Kang, Z.Q., 2021. Evolution of permeability and mesostructure of oil shale exposed to high-temperature water vapor. Fuel 290, 119786. https://doi.org/10.1016/j.fuel.2020.119786.
- Wang, L., Yang, D., Zhang, Y.X., et al., 2022. Research on the reaction mechanism and modification distance of oil shale during high-temperature water vapor pyrolysis. Energy 261, 125213. https://doi.org/10.1016/j.energy.2022.125213.
- Xu, Q.H., Long, W., Jiang, H., et al., 2018. Pore-scale modelling of the coupled thermal and reactive flow at the combustion front during crude oil in-situ combustion. Chem. Eng. J. 350, 776–790. https://doi.org/10.1016/ j.cej.2018.04.114.
- Yuan, C.D., Pu, W.F., Ifticene, M.A., et al., 2022. Crude oil oxidation in an air injection based enhanced oil recovery process: chemical reaction mechanism and catalysis. Energy & Fuels 36 (10), 5209–5227. https://doi.org/10.1021/ acs.energyfuels.2c01146.
- Zhang, Y., Huang, S.Y., Sheng, J.J., et al., 2020. Experimental and analytical study of oxygen consumption during air injection in shale oil reservoirs. Fuel 262, 116462. https://doi.org/10.1016/j.fuel.2019.116462.
- Zhao, R.B., Chen, Y.X., Huan, R.P., et al., 2015. An experimental investigation of the in-situ combustion behavior of Karamay crude oil. J. Petrol. Sci. Eng. 127, 82–92. https://doi.org/10.1016/j.petrol.2015.01.005.
- Zhao, R.B., Sun, Z.Q., Yang, F.X., et al., 2023. A dynamic control strategy for improving combustion chamber sweep efficiency during the in-situ combustion. Appl. Therm. Eng. 235, 121439. https://doi.org/10.1016/ j.applthermaleng.2023.121439.
- Zhao, S., Xu, C.Y., Pu, W.F., et al., 2021a. Oxidation characteristics and kinetics of shale oil using high-pressure differential scanning calorimetry. Energy & Fuels 35 (22), 18726–18732. https://doi.org/10.1021/asc.energyfuels.1c02854.
- Zhao, S., Pu, W.F., Su, L., et al., 2021b. Properties, combustion behavior, and kinetic triplets of coke produced by low-temperature oxidation and pyrolysis: implications for heavy oil in-situ combustion. Petrol. Sci. 18 (5), 1483—1491. https://doi.org/10.1016/j.petsci.2021.08.005.
- Zhao, S., Pu, W.F., Varfolomeev, M.A., et al., 2022. Influence of water on thermooxidative behavior and kinetic triplets of shale oil during combustion. Fuel 318, 123690. https://doi.org/10.1016/j.fuel.2022.123690.
- Zhao, S., Pu, W.F., Jiang, Q., et al., 2023a. Investigation into the key factors influencing the establishment and propagation of combustion front in ultra-deep high-temperature heavy oil reservoirs. Energy 283, 129017. https://doi.org/10.1016/j.energy.2023.129017.
- Zhao, S., Pu, W.F., Li, Y.B., et al., 2023b. Low-temperature oxidation characteristics and reaction pathways of crude oil within tight shale during air injection. Petroleum. https://doi.org/10.1016/j.petlm.2023.12.005.
- Zhao, S., Pu, W.F., Chen, Q.Y., et al., 2024a. Propagation of combustion front within fractured shale and its influence on shale structure and crude oil properties: an experimental study. SPE J. 29 (5), 2389–2398. https://doi.org/10.2118/219456-PA.
- Zhao, S., Pu, W.F., Li, Y.B., et al., 2024b. Oxidation behavior and kinetics of shale oil under different oxygen concentrations. Fuel 361, 130677. https://doi.org/ 10.1016/j.fuel.2023.130677.
- Zhou, G.Z., Guo, Z.Q., Sun, S.M., et al., 2023a. A CNN-BiGRU-AM neural network for AI applications in shale oil production prediction. Appl. Energy 344, 121249. https://doi.org/10.1016/j.apenergy.2023.121249.
- Zhou, S.M., Huang, L.K., Wang, G.Z., et al., 2023b. A review of the development in shale oil and gas wastewater desalination. Sci. Total Environ. 873, 162376. https://doi.org/10.1016/j.scitotenv.2023.162376.